Carbohydrate Polymers 308 (2023) 120622

Contents lists available at ScienceDirect

Carbohydrate Polymers

journal homepage: www.elsevier.com/locate/carbpol

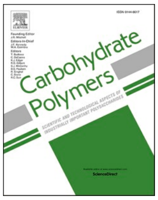

Percolation and phase behavior in cellulose nanocrystal suspensions from nonlinear rheological analysis

Sylwia Wojno[a,b], Astrid Ahlinder[c], Annika Altskär[c], Mats Stading[a,c], Tiffany Abitbol[d,*], Roland Kádár[a,b,**]

[a] Chalmers University of Technology, Industrial and Materials Science, SE-412 96 Gothenburg, Sweden
[b] Wallenberg Wood Science Centre (WWSC), Chalmers University of Technology, SE-412 96 Gothenburg, Sweden
[c] RISE, Research Institutes of Sweden AB, Agriculture and Food, SE-412 76 Gothenburg, Sweden
[d] EPFL, Institute of Materials, School of Engineering, Lausanne 1015, Switzerland

ARTICLE INFO

Keywords:
Cellulose nanocrystal suspensions
Percolation
Self-assembly phases
Fourier-transform rheology
Stress decomposition

ABSTRACT

We examine the influence of surface charge on the percolation, gel-point and phase behavior of cellulose nanocrystal (CNC) suspensions in relation to their nonlinear rheological material response. Desulfation decreases CNC surface charge density which leads to an increase in attractive forces between CNCs. Therefore, by considering sulfated and desulfated CNC suspensions, we are comparing CNC systems that differ in their percolation and gel-point concentrations relative to their phase transition concentrations. The results show that independently of whether the gel-point (linear viscoelasticity, LVE) occurs at the biphasic - liquid crystalline transition (sulfated CNC) or at the isotropic - quasi-biphasic transition (desulfated CNC), the nonlinear behavior appears to mark the existence of a weakly percolated network at lower concentrations. Above this percolation threshold, nonlinear material parameters are sensitive to the phase and gelation behavior as determined in static (phase) and LVE conditions (gel-point). However, the change in material response in nonlinear conditions can occur at higher concentrations than identified through polarized optical microscopy, suggesting that the nonlinear deformations could distort the suspensions microstructure such that for example a liquid crystalline phase (static) suspension could show microstructural dynamics similar to a biphasic system.

1. Hyphothesis

We hypothesize that anomalous nonlinear material signatures correspond to both (i) weak percolation and (ii) phase behavior in self-assembling CNC suspensions. By comparing sulfated and desulfated CNC suspensions we compare systems with different percolation theresholds relative to phase transition concentrations.

2. Introduction

Cellulose nanocrystals (CNCs) can be approximated as rod-shaped nanoparticles generally prepared by controlled acid hydrolysis (Habibi et al., 2010). Their characteristic dimensions depend on cellulose source and hydrolysis method (Dong et al., 1998; Dufresne, 2017). The type of acid used for extraction greatly affects the suspension stability of CNCs and their surface charge density. For example, due to the grafting of negatively charged sulfate half esters onto the surface of CNCs, hydrolysis with sulfuric acid leads to electrostatically stabilized dispersions. For sulfated CNC suspensions the dominant forces are repulsive CNC-CNC interactions (Dufresne, 2017). Uncharged CNCs can be obtained by cellulose hydrolysis with hydrochloric acid (Araki et al., 1998). However, this uncharged system is highly unstable and tends to aggregate, which makes these CNCs undesirable for most applications. A route to CNCs with low or intermediate surface charge densities is by desulfation. CNCs obtained in this method are colloidally stable compared to extraction with hydrochloric acid. Sulfate half-ester groups can be removed by acid- or alkali de-esterification at a temperature above 50°C (Jiang et al., 2010). In uncharged or low surface charge systems, attractive van der Waals forces dominate (Araki, 2013; Xu et al., 2018). This affects the stability of aqueous CNC suspensions and their self-assembly properties. Simultaneously, the viscosity of desulfated CNCs systems greatly increases (Abitbol et al., 2018; Araki et al., 1999).

---

* Correspondence to: T. Abitbol, EPFL, Institute of Materials, School of Engineering, Lausanne 1015, Switzerland.
** Correspondence to: R. Kádár, Chalmers University of Technology, Industrial and Materials Science, SE-412 96 Gothenburg, Sweden.
E-mail addresses: tiffany.abitbol@epfl.ch (T. Abitbol), roland.kadar@chalmers.se (R. Kádár).

https://doi.org/10.1016/j.carbpol.2023.120622
Received 5 November 2022; Received in revised form 11 January 2023; Accepted 22 January 2023

The hierarchical structure and self-assembly of CNCs depends on many factors. For example, Dong et al. (1996) investigated the impact of ionic strength on the liquid crystalline phase behavior of CNC suspensions, concluding that a decrease in double-layer thickness increases chiral interactions between CNCs. Shafiei-Sabet et al. (2014) studied the effect of electrolytes on ionic strength and rheological properties. In later studies by the same group, Shafeiei-Sabet et al. (2013) investigated the effect of surface charge and concentration on the self-assembly of CNCs. They found that the degree of sulfation has a significant impact on critical transition concentrations of the suspensions, i.e. from isotropic, through biphasic, liquid crystalline and up to an arrested repulsive phase. A similar study was performed by Abitbol et al. (2018), who interpreted the rheological properties of the investigated suspensions in terms of the increase in double-layer thickness that occurs with decreasing surface charge. In turn, Xu et al. (2017) applied rheology to characterize surface-sulphated NCC suspensions as a function of pH, salinity (NaCl) and NCC concentration. Based on this extended study they elaborated a phase diagram of CNC suspensions as a function of CNC concentration and solution ionic strength (Xu et al., 2020).

Polarized Light Imaging (PLI) is a straightforward way to visualise the orientation dynamics of CNC assemblies while simultaneously performing rheological measurements (Kádár et al., 2021). The main challenge of understanding the flow dynamics of CNC suspensions lies in resolving their hierarchical behavior in flow. Rheology is a comprehensive measurement technique that captures all levels of a material hierarchy within the bulk material response. To elucidate the dynamics of a material hierarchy in flow, the most promising approach remains combining rheological methods with other analytical techniques(Kádár et al., 2021), simultaneously or complementary. It should be noted that each analytical approach has advantages and limitations in applicability, spatio-temporal scaling and material properties that can be investigated. We note that rheo-PLI is the most readily available optical method, while at the same time the most challenging for microstructural quantification. In addition, advancements in nonlinear rheological analysis have been recently applied to CNC suspensions, with the advantage of increased measurement sensitivity and the potential to reveal material response features that are not observable in standard linear viscoelastic measurements (Abbasi Moud et al., 2020; Moud et al., 2021; Wojno et al., 2019; Wojno et al., 2022). Abbasi et al.(Abbasi Moud et al., 2020) studied the effect of NaCl on the changes in the microstructure of CNC suspensions via nonlinear viscoelastic analysis. Another study using this technique detected the formation of a double network in CNC-PVA (polyvinyl alcohol)/salt hydrogels (Moud et al., 2021). In our previous work, we studied for the first time the relationship between nonlinear material parameters and the phase behavior of CNC suspensions (Wojno et al., 2022). Carlos and Walter (2021) investigated the transition from Linear Visco-Elastic (LVE) to Large Amplitude Oscillatory Shear (LAOS) region depending on the concentration and pH of carboxymethyl cellulose gels. On the other hand Fourier - Transform (FT) rheology technique was applied to Cellulose nanofibers (CNF) suspensions, which revealed that the nonlinear viscoelastic properties reflected both effects of chemical pretreatments and mechanical fibrillation (Song et al., 2022).

In this work, we investigate for the first time the impact of the surface charge of CNCs on nonlinear rheological properties via nonlinear oscillatory shear analysis and rheo-PLI. We complement the advanced rheological analysis with polarized optical microscopy (POM) and transmission electron microscopy (TEM) analysis of the CNC suspensions structure at rest. The study complements previous reports on the influence of surface charge on the linear viscoelastic and steady shear rheological behavior of CNCs (Abitbol et al., 2018; Hausmann et al., 2018; Shafeiei-Sabet et al., 2013; Shafiei-Sabet et al., 2014). By varying the surface charge we can examine the relationship between nonlinear material parameters and the percolation threshold, the formation of a rheological gel and the transition between CNC phases. Our overarching goal is to elucidate the microstructural origin of anomalous nonlinear material response, so-called nonlinear "oddities", characteristic of CNC suspensions.

3. Experimental section

3.1. Materials

All suspensions were prepared from spray dried cellulose nanocrystals purchased from Celluforce, CELLUFORCE NCV100 – NASD90 (Montreal, Canada), see Fig. 1. A stock suspension at 2 wt% CNC concentration was prepared with Milli-Q water (Millipore Milli-Q Purification System) and dispersed by microfluidization (M110-EH, 1700 bar, 1 pass), followed by filtration twice through Munktell Filtrak™ grade 3 papers (Fischer Scientific). Next, the 2 wt% CNC stock suspension was gently evaporated at room temperature with magnetic stirring until 10.2 wt%. Concentrations of 2, 3 and 5 wt% CNC were prepared from the 10.2 wt% suspension by dilution with deionized water (Millipore Milli-Q Purification System) and magnetic stirring at room temperature for 24 h, Fig. 1. Low charge CNC suspensions were prepared from the 2 wt% Na-form stock CNC suspension by an acid catalyzed desulfation as has been previously reported (Abitbol et al., 2013). After extensive dialysis, the acid-form desulfated CNCs were exchanged to their sodium form by the addition of NaOH to a pH of 7 and upconcentrated to 1.45 wt %. Thereafter, the $1.45^{'D}$ wt% CNC suspension was diluted with Milli-Q water to $0.5^{'D}$ and $0.73^{'D}$ wt%, Fig. 1. Sulfated and desulfated CNC dispersions couldn't be compared at the same concentrations due to different surface charges resulting in a higher aspect ratio for the latter ones. Therefore, we selected different concentrations to estimate the percolation threshold, gelation and phase transitions for these two different CNC systems.

3.2. Dynamic Light Scattering (DLS) and Zeta potential

Dynamic Light Scattering (DLS) and zeta potential measurements of CNC suspensions were performed using a Zetasizer Nano ZS (Malvern Instruments, UK) and DTS1070 folded capillary cells. CNC suspensions were diluted to 0.001 wt% for DLS and 0.01 wt% for zeta potential, at an NaCl concentration of 1 mM, which was added to compress the electrical double layer (Qi et al., 2005; Reid et al., 2017). All measurements were conducted at 25 °C, with a stabilization time of 120 s, repeated 3 times and the average value was reported.

3.3. Conductometric titration

Surface charge was measured using conductometric titration. Acid-form CNC suspensions in the presence of NaCl were titrated against NaOH. The inflection point from the titration can be related to the surface charge density of crystallites (Dong et al., 1998), i.e. percent sulfur content by weight, calculated as:

$$\%S \equiv \frac{V_{NaOH} C_{NaOH} M_w(S)}{m_{susp} C_{susp}} \times 100\% \tag{1}$$

where V_{NaOH} corresponds to the volume of NaOH at the equivalence point, C_{NaOH} is the concentration of NaOH used to the conductometric titration, $M_w(S)$ refers to the molecular weight of sulfur, and m_{susp} and C_{susp} are the mass and concentration of the suspension, respectively.

3.4. Polarized optical microscopy (POM)

Transmission optical microscopy was carried out with a Zeiss axioplan (Oberkochen, Germany) optical microscope with 10× objective equipped with linear polarizers in a cross-polarizer setup with a 530 nm phase retardation plate. Due to the retardation plate, the isotropic phase can be identified as bright pink and oriented (mesophase) regions, as different than pink.

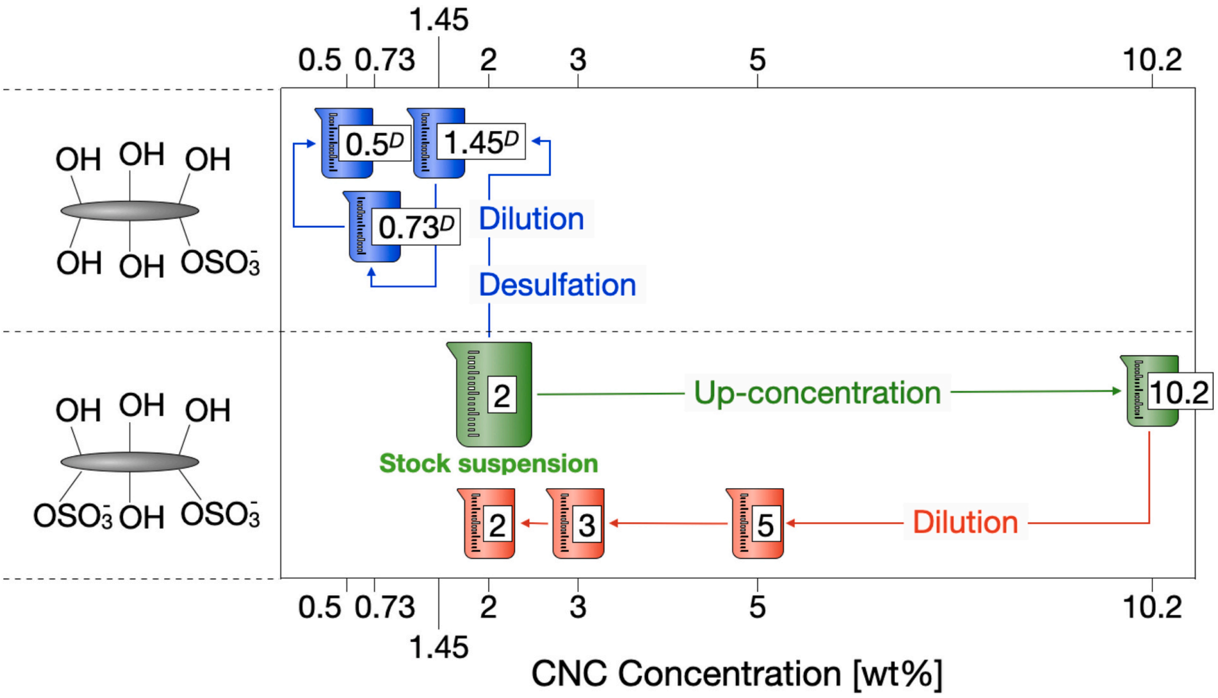

Fig. 1. Schematic overview of CNC suspensions characterized.

3.5. Transmission electron microscopy (TEM), freeze substitution and embedding

Small droplets of the CNC suspensions (maximum of 1 mm^3) were rapidly frozen in liquid ethane/propane, then transferred to a freeze substitution AFS2 FSP equipment chamber (Leica, Wetzlar, Germany) kept at −90 °C. Water is substituted with acetone at −40 °C, followed by substitution with ethanol prior to infiltration with Lowicryl HM20 (EMS, Hatfield, PA, United States). The resin was polymerized at −40 °C using UV-light and ultrathin sections of 60 nm of each sample was performed using a Diatome ultra diamond knife (Diatome, Hatfield, PA, United States) in a Powertome XL ultramicrotome (RMC products, Boeckeler Instruments Inc., Tucson, Arizona, United States). Analyses were made of the sulfated CNCs at 3.9 and 10.2 wt% suspensions, in addition to the desulfated CNCs at 0.77$^{\prime D}$ and 1.45$^{\prime D}$ wt%.

3.6. Rheological characterization

All rheological measurements were performed on an Anton Paar MCR 702e Space MultiDrive rheometer (Graz, Austria) at 23 °C with a parallel plate measuring system. Before testing, each sample was allowed to relax for 60 s after moving to the gap position (0.9–1 mm depending on the concentration). Two sets of configurations were used: (i) a single motor-transducer setup for rheo-PLI and (ii) a separate motor-transducer setup for nonlinear oscillatory shear analysis.

3.7. Rheo-PLI

Rheo-PLI experiments were performed in a single motor transducer configuration using a custom rheo-optical visualization setup based on the P-PTD200/GL accessory with a parallel-plate geometry of ($2 \cdot R =$)43 mm diameter. Two linear polarizers were placed at 45° relative orientation above and below the parallel-plate setup. More details about the setup, including the construction of space-time diagrams, can be found in other publications (Kádár, Fazilati, & Nypelö, 2020; Wojno et al., 2022; Fazilati et al., 2021), while a schematic diagram of the setup can be found in Fig. SI1 (Supplementary information). Both oscillatory and steady shear measurements were performed on this setup. The strain sweep measurements were performed at 1 rad/s with the strain amplitude ranging from 0.01 to 1500 %. In turn, the steady shear measurements were conducted within the shear rate range of 0.01 to 100 s^{-1} using a custom procedure for steady-state detection (Kádár, Fazilati, & Nypelö, 2020; Fazilati et al., 2021).

3.8. Nonlinear oscillatory shear analysis

Linear and nonlinear oscillatory shear measurements were performed using a parallel-plate geometry of ($2 \cdot R =$)50 mm in diameter in strain controlled mode (separate motor-transducer), with 0.9–1 mm gap (depending on concentration). Strain sweep measurements were performed within a strain amplitude range of 0.1 to 1500 % at 4 different angular frequencies: 0.6, 1, 2 and 4 rad/s. For 2 wt%, strain sweep measurements were performed within a higher strain range, 0.1 to 10,000 % using a cone-plate geometry (2 °) of the same diameter. Frequency sweep tests were performed between 0.1 and 628 rad/s at an imposed strain amplitude of 1 %.

The nonlinear analysis of the shear stress output was performed in the framework of Fourier-Transform and stress decomposition analyses. In nonlinear conditions, the stress output signal is non-sinusoidal, which results in higher harmonics in the corresponding Fourier spectra, in addition to the fundamental intensity, I_k, $k = 3, 5\ldots$ (Hyun et al., 2011), see Fig. SI2(b). The third relative higher harmonic, $I_{3/1} \equiv I_3/I_1$, can be used to characterize the shear stress signal nonlinearities. In the linear viscoelastic regime, at small strain amplitudes (small amplitude oscillatory shear, SAOS), $I_{3/1} \propto \gamma_0^{-1}$ which refers to nonlinearities due to instrumentation noise (Hyun et al., 2011). Increasing strain amplitude leads to the medium amplitude oscillatory shear (MAOS) that results in an increase in $I_{3/1}$ response, where $I_{3/1} \propto \gamma_0^2$ (Hyun & Kim, 2011). The scaling exponent $n = 2$, where $I_{3/1} \propto \gamma_0^n$, can be deduced theoretically from matching the Taylor series of the shear stress output to the corresponding Fourier series, and is found experimentally directly in most simple cases, e.g. see Fig. SI2(c), or it is assumed that $I_{3/1}$ can be extrapolated thereto(Hyun et al., 2011). Further increasing the strain amplitude, i.e. large amplitude oscillatory shear (LAOS), leads to the loss of quadratic scaling. Additional nonlinear parameters can be also calculated from the intra-cycle behavior of the shear stress, as represented by Lissajous-Bowditch diagrams, and are briefly described in the supplementary information.

4. Results and discussion

First, we make here a few nomenclature notes from a rheological perspective. In this publication we refer to "percolation threshold" (ϕ_c) as the lowest concentration at which a CNC suspension has an elastically dominated rheological response, i.e. $G' \geq G''$. We refer to a material response for which $G' \geq G''$ as having a "gel-like" behavior. Note that this includes weakly percolated networks, where an increase in ω can disrupt the percolated network leading to a liquid-like behavior, $G' < G''$. We refer to the gel point (ϕ_g) as defined by Winter and Chambon (1986) whereby the dynamic moduli are approximately equal, $G' \approx G''$ and G', $G'' \sim \omega^{\alpha}$, within the angular frequency range investigated. Therefore the term 'gel' can be associated to the isotropic, biphasic and liquid crystalline phases depending on sample preparation and surface charge. Note that in this context referring to arrested states for concentrations above the liquid crystalline phase can be confusing. We also wish to highlight that the customary denominations of CNC suspension phases, i.e. "isotropic", "biphasic", "quasi-biphasic" and "liquid crystalline" are characteristic of suspensions at rest (no flow). However, we use their designations only indicative of the expected interaction during flow. In particular, the term "biphasic" refers to the co-existence of both liquid crystalline and isotropic domains(Parker et al., 2018) and is usually determined based on phase separation when a suspension is allowed to settle at rest. For the desulfated systems investigated, that contain co-existing liquid crystalline and isotropic domains, without visible macro-scale phase separation when allowed to settle, we use the term "quasi-biphasic".

4.1. Morphological characterization

The physico-chemical analysis of both CNC systems is summarized in Table 1. The apparent particle size by light scattering gave a characteristic size for the sulfated CNCs of 62.8 ± 0.2 nm, while desulfated CNCs were almost 3 times larger, i.e. 180.9 ± 9.1 nm. This can be explained by strong attractive interactions overcoming repulsive forces resulting in agglomeration that results in a larger apparent size. The acid desulfation decreased the surface charge density, as expressed by the reduction in sulfur content, from 0.81 ± 0.05 % to 0.26 ± 0.08 %. Both CNC systems had an average zeta potential typical for macroscopiccally stable colloidal suspensions. Bhattacharjee (2016) has deduced that absolute values of > 30 mV indicate highly stable CNC colloids in the presence of NaCl. Therefore, reducing the surface charge for the desulfated CNC system, decreased their stability slightly. The aspect ratio was also estimated from rheological data and the description thereof can be found in the Supplementary information.

4.2. Polarized optical microscopy

Polarized optical micrographs of sulfated and desulfated CNC dispersions are presented in Fig. 2, mainly as means to independently asses the phase of the CNC suspensions analyzed. It should be noted that the use of the phase retardation plate alters the color palette, and therefore for comparison Fig. SI4 contains POM of the same samples in the absence of the retardation plate. The sulfated CNC suspension with the lowest concentration, 2 wt%, appears bright pink in Fig.2, which has been assigned to the isotropic phase (Abitbol et al., 2013). Corroborated by POM in Fig. SI4, the 3 wt% suspension shows the beginning of liquid crystalline domain assembly as inferred by the weak coloring. Concentrations of 5 and 10.2 wt% showed the fingerprint texture distinctive of chiral nematic liquid crystals in Fig. 2. Furthermore, the micrograph of the 10.2 wt% suspension shows a crosshatch pattern. A similar observation was made by Araki et al. (2000) who observed a crosshatch pattern for a 7.1 wt% postsulfated CNC suspension. They indicated that this pattern is reminiscent of a "frozen-in shear structure" in the "birefringent glassy phase", which can be found in the aqueous suspensions of boehmite rods (Buining et al., 1994) or clay (Gabriel et al., 1996). Long-range repulsive interactions cause immobilization of the bohemite systems, which results in a crosshatch pattern. The similar pattern observed for the 10.2 wt% sulfated CNC suspension could be the result of a very high viscosity, which causes the structure to be built of numerous small domains, each of which presents a different birefringence pattern. We note, that a crosshatch pattern was also reported by Bercea and Navard (2000), for non-arrested states but in shear flow during rheo-PLI measurements. The identified phases are similar to the study of Dong et al. (1996) on a different sulfated CNC system, who indicated that for pure sulfated CNC suspensions, the isotropic phase is below 3.6 wt% and biphasic phase between 3.6 and 4.7 wt% CNC. The lowest desulfated concentration, $0.5^{'D}$ wt% CNC, shows a similar bright pink coloring as in Fig. 2(a) micrograph characteristic of the isotropic phase. $0.73^{'D}$ wt% CNC, while predominantly bright pink, it shows some orientation in the vicinity of air bubble induced curvatures, see also Fig. SI4, while $1.45^{'D}$ wt% CNC appeared more birefringent than the lower desulfated concentrations. The lack of visible phase separation makes the term "quasi-biphasic" more appropriate for those desulfated CNC suspensions which exhibit birefringence properties.

Table 1
Physico-chemical properties of CNC suspensions.

	DLS size [nm]	Predicted *L*/*D*	ζ-potential [mV]	Sulfur [%]
Sulfated CNCs	62.8 ± 0.2	65.9	46.4 ± 0.4	0.81 ± 0.05
Desulfated CNCs	180.9 ± 9.1	185.4	31.8 ± 0.7	0.26 ± 0.08

4.3. Transmission electron microscopy (TEM)

In Fig. 3 micrographs of sulfated and desulfated CNC dispersions are shown for the concentrations of 3.9 wt%, 10.2, $0.77^{'D}$ and $1.45^{'D}$ wt%, aiming to visualise the primary CNC nanoparticles and their network formation. At 3.9 wt%, a fine network of interconnected rods is seen while not as distinct for $0.77^{'D}$. In Fig.3 (d) with $1.45^{'D}$ wt% larger aggregates are seen, viewed as thicker strands despite the individual rods having the same size as the sulfated CNC in (c). Additionally, indications of an end to end aggregation can be seen in (d) arranged in a planar nematic structure. The aggregation of the individual rods arise from the reduced surface charge resulting in a larger apparent size as seen by DLS in Table 1. In Fig.3 (b) the concentration of 10.2 wt% results in a dense, highly packed network which is more finely dispersed in space due to the higher surface charge of the CNCs. This makes the network structure less distinct at 10.2 wt% at this high magnification. For 3.9 wt% the suspension vial was kept at rest until phase separation occurred and the sample taken from the anisotropic bottom phase. As expected no biphasic separation was seen in the vial for $0.77^{'D}$ during inital trials, and the sample was thus analyzed after being at rest over night, the sample taken from the bottom part of the vial. The micrographs were prepared from samples that were fixed in their native state using freeze substitution. This reduces artifacts from drying effects often seen of TEM micrographs of dried films (Kaushik et al., 2014). Despite the wide difference in concentration range between the sulfated and desulfated samples these micrographs show network formation at the selected concentrations.

4.4. Steady and oscillatory shear tests

Fig. 4 shows the steady shear viscosity functions for all investigated CNC suspensions. In the case of sulfated CNC suspensions, 2 and 3 wt% exhibited a zero-shear viscosity Newtonian plateau followed by a shear-

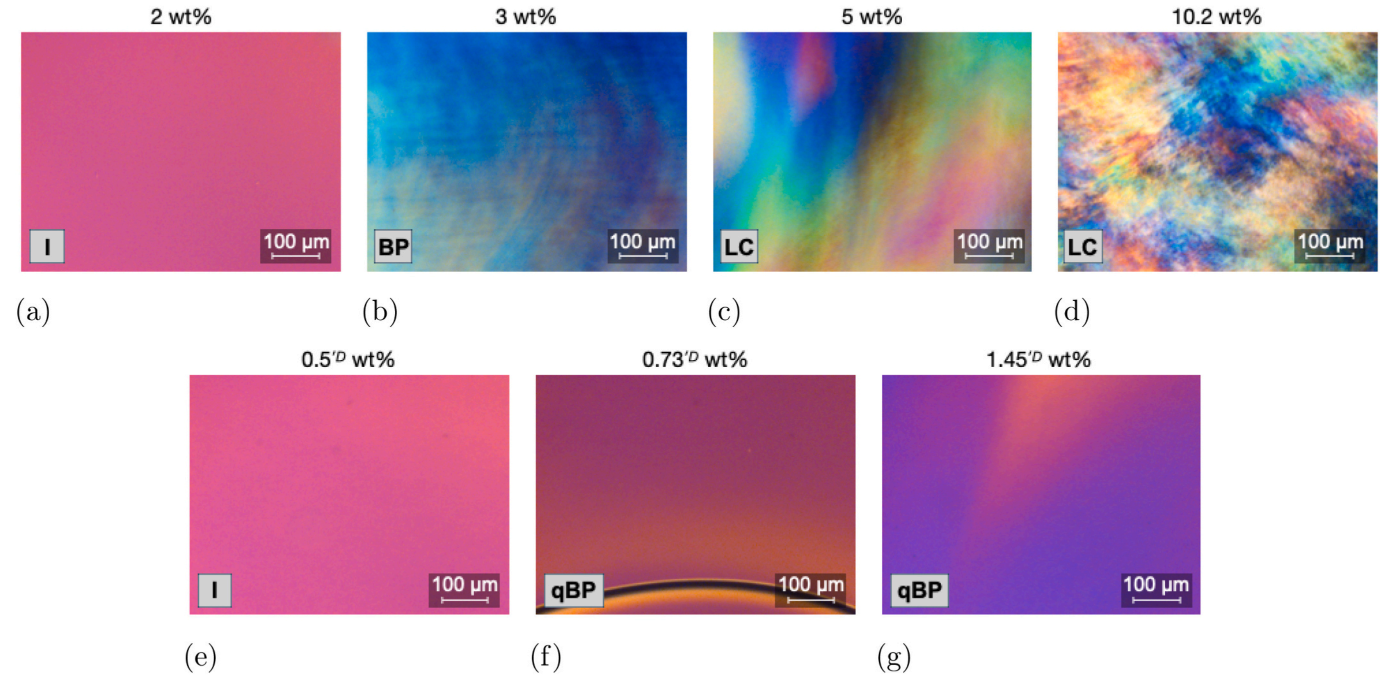

(a) (b) (c) (d)

(e) (f) (g)

Fig. 2. Polarized optical micrographs (POM) of the CNC suspensions studied at rest, (a)-(d) sulfated and (e)-(g) desulfated CNC dispersions.

thinning region. As concentration increases, the so-called three-region behavior, characteristic of liquid-crystalline systems(Onogi & Asada, 1980), could be observed. Such is the case for 5 wt%, while 3 wt% shows evidence of a three-region viscosity function behavior, although not as clearly defined as for 5 wt%. Depending on the CNC systems investigated, the three-region shear viscosity functions has been assigned to biphasic (Ao et al., 2011), liquid-crystalline(Orts et al., 1998; Shafeiei-Sabet et al., 2013; Shafiei-Sabet et al., 2012) or both phases (Haywood et al., 2017; Wojno et al., 2022). Fig.4(b) shows examples of PLI flow visualizations (still frames) at the transition to different regions for 5 wt % with increasing shear rate. Polarized light combined with polarizers helps to observe and identify crystalline, oriented structures. This pattern indicates a parallel orientation of one of the main axes of the optical indicatrices of a birefringent material (CNC) in the plane of polarization of the incident light (Völker-Pop, 2014). At the scale of the PLI visualization, in region (i) the color patterns remain virtually unchanged which suggests that shear thinning in this region is associated to structural re-arrangements below the observation scale. An increase in anisotropy with increasing shear rate has been seen in region (i) using rheo-SANS (Haywood et al., 2017; Kádár et al., 2021). In region (ii), a region associated with a relatively constant anisotropy (Haywood et al., 2017), significant color distortions can be observed, including the presence of radial birefringence patterns (Kádár, Fazilati, & Nypelö, 2020), which will be discussed further in the text. In region (iii), where a predominant orientation in the flow direction is expected (Haywood et al., 2017), PLI visualizations clearly show a Maltese-cross pattern. The highest investigated sulfated CNC concentration, 10.2 wt% exhibited a single shear-thinning region. In the desulfated suspensions, the isotropic $0.5^{\prime D}$ wt% behaved qualitatively similar to the isotropic sulfated 2 wt%. The three times higher effective aspect ratio of the desulfated suspensions can be readily observed as an approximately one order of magnitude higher zero-shear viscosity for the $0.5^{\prime D}$ wt% at a low shear rate followed by a shear-thinning region. Quasi-biphasic $0.73^{\prime D}$ wt% exhibited zero-shear viscosity followed by shear-thining behavior similar to 3 wt% biphasic CNC. The desulfated quasi-biphasic $1.45^{\prime D}$ wt % CNC showed one shear thinning region, similar to the sulfated liquid crystalline suspensions, however, one order of magnitude lower than the highest sulfated concentration, 10.2 wt%. We note that while both $0.73^{\prime D}$ and $1.45^{\prime D}$ wt% are quasi-biphasic, they differ in terms of gel behavior, see the linear viscoelastic oscillatory shear analysis ahead.

Fig. 5 contains the space-time diagrams corresponding to the rheo-PLI tests in Fig. 4(a), while visualizations at the selected shear rates can be found in Fig. 6. As expected, the most diluted CNC systems, both isotropic sulfated, 2 wt%, and desulfated, $0.5^{\prime D}$ wt%, showed no discernible change in birefringence patters for the full range of shear rates investigated. As concentration increases, the degree of local order in the suspensions increases, which results in color development, and the presence of a Maltese cross with increasing shear rate. Thus, suspensions containing the beginnings of liquid crystalline assembly, sulfated 3 wt% and desulfated $0.73^{\prime D}$ wt% and $1.43^{\prime D}$, share a common color palette of brown - blue. The higher the CNC-CNC interactions, as evidenced by viscosity, the more likely colors are distinguishable before the application of a shear flow with no colors detected for 3 wt% and both blue and brown visible for $1.45^{\prime D}$. Viscosity plays a determinant role also on the orientation dynamics, with $1.45^{\prime D}$ experiencing a chromatically homogenous Maltese-cross pattern for $\dot{\gamma} \geq 1.2$ 1/s compared to 3 wt% and $0.73^{\prime D}$ wt% where the same pattern can be observed for $\dot{\gamma} \geq 0.3$ 1/s. No Maltese-cross color change was recorded for desulfated CNCs, whereas sulfated 3 wt% Maltese-cross changes color from a brown to a blue color with increasing shear rate, similar to previous observations Fazilati et al. (2021). Sulfated 5 wt% and 10.2 wt% displayed significant initial ($\dot{\gamma} = 0$) isochromatic areas and color changes with increasing shear rate, characteristic of liquid crystal phases (Kádár, Fazilati, & Nypelö, 2020; Wojno et al., 2022). Interestingly, for sulfated 5 wt% CNC in the shear rate range $\dot{\gamma} \in (0.05, 0.5)$ 1/s a radially periodic birefringence pattern was detected, see Fig. SI5. Such patterns were first observed in CNC-based suspensions by Kádár, Fazilati, and Nypelö (2020) also in a 5 wt % suspension and at comparable shear rates. More recently, Wychowaniec et al. (2021) reported virtually identical birefringence patterns in graphene oxide (lyotropic liquid crystals) suspensions and spatially resolved the flow structure to a form of elastic instabilities, whereby the radial 'bands' correspond to toroidal vortices (Wychowaniec et al., 2021). Based on a visual similarity and given that our shear rate range corresponds to Reynolds numbers $Re \in (6 \cdot 10^{-6}, 6 \cdot 10^{-5})$ and Péclet numbers $Pe \in (5 \cdot 10^{4}, 5 \cdot 10^{5})$ (for definitions please see Eq. SI 6–7 in the Supplementary Information), we conjecture that the radial birefringence

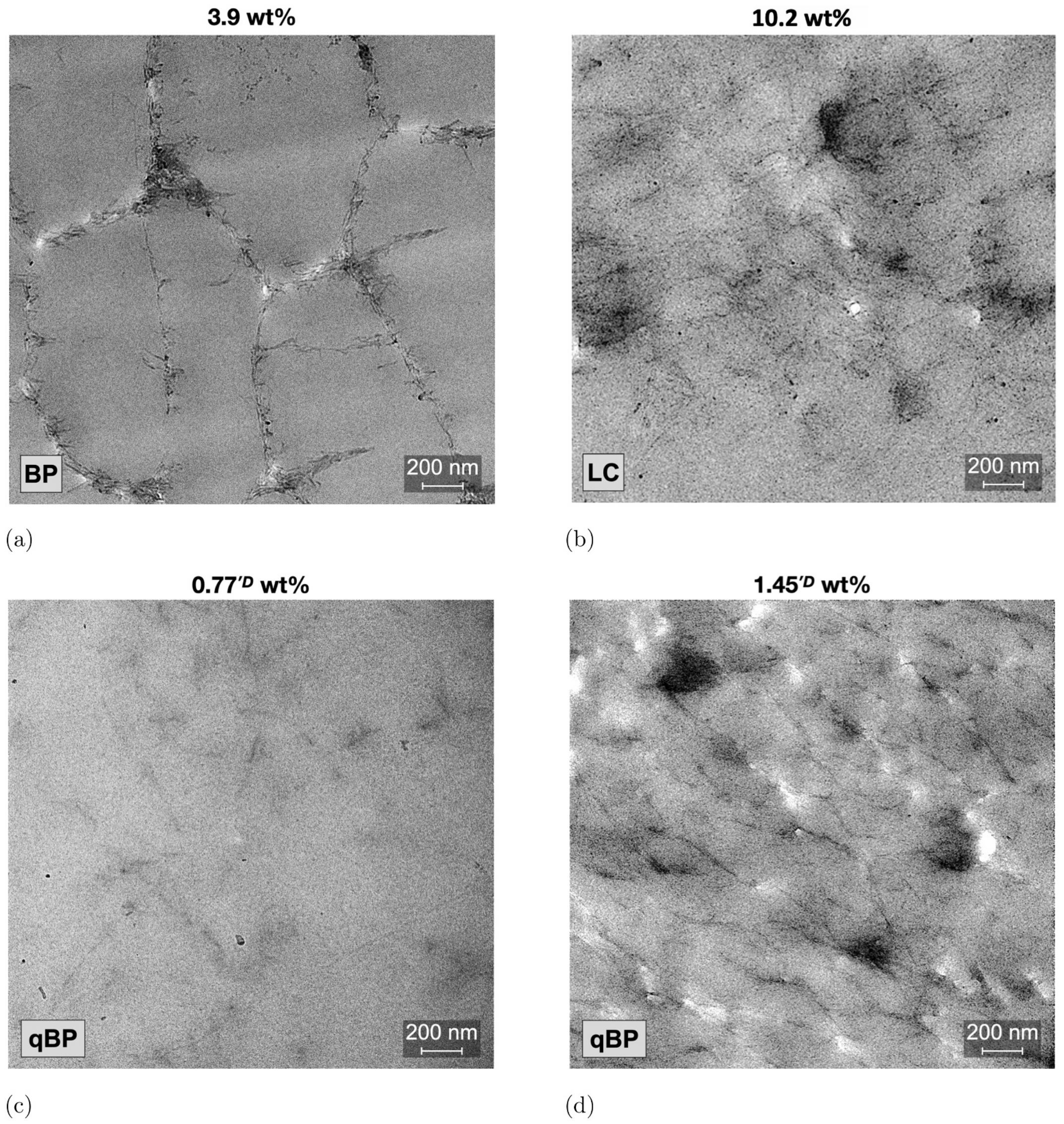

(a) (b) (c) (d)

Fig. 3. TEM micrographs of (a) 3.9 wt% and (b) 10.2 wt% and (c) $0.77^{'D}$ wt% (d) $1.45^{'D}$ wt%.

patterns we observe in CNC suspensions are also a form of elastic instabilities. We note that 3 wt% CNC also presents a three-region viscosity function but no radial birefringence patterns. For 5 wt%, the blue/purple colored Maltese-cross at onset (approximately $\dot{\gamma} \geq 1.2$ 1/s switches to a green / pink coloration. In contrast, 10.2 wt% exhibited an inhomogeneous Maltese-cross pattern for $\dot{\gamma} \geq 23$ 1/s. The lack of color homogeneity can be attributed to the presence of radial birefringence patterns for $\dot{\gamma} \geq 23$ similar to the phenomena described for 5 wt%.

Dynamic frequency sweep measurements are shown in Fig. 7, see also Fig. SI6–7 (Supplementary information). Sulfated CNC suspensions, concentrations <5 wt% showed liquid-like behavior, with $G'' > G'$, while the liquid crystalline 5 wt% is at the rheological gel point, with $G' \approx G''$. The liquid crystalline concentration, 10.2 wt%, showed a gel-like behavior with a significant weak strain overshoot (WSO) in the strain sweep data, whereby G'' locally increases at the transition to the nonlinear viscoelastic regime. The isotropic desulfated $0.5^{'D}$ wt% CNC was characterized by very close dynamic moduli values, with a slight G'' $> G'$ behavior. Desulfated CNC $>0.5^{'D}$ exhibited gel-like behavior, $G' >$ G'' over the entire tested frequency range. Additionally, they also exhibited WSO in strain sweep tests. The WSO was significantly more pronounced with increasing concentration, as expected. Overall, we can state that gel point, defined for states where $G' = G'' \neq f(\omega)$ Winter and Chambon (1986), for desulfated CNC suspensions is likely slightly higher than $0.5^{'D}$ wt% (considering both strain sweep and frequency sweep results) and for sulfated CNC suspensions it is around 5 wt% CNC. An important aspect to highlight is that a rheological gel state is detected for desulfated systems in the isotropic - quasi-biphasic transition region, while for the sulfated systems it is at the biphasic - liquid crystalline transition region.

4.5. *Nonlinear oscillatory shear analysis and comparison with rheo-PLI*

In this paragraph we refer mainly to the nonlinear material response as expressed by the third relative higher harmonic, $I_{3/1}$, for brevity and for being the most basic quantity, yet one of the most versatile, that characterizes nonlinearities in shear stress. In addition, stress decomposition analysis results are included in the Supplementary Information and are briefly described. The results are discussed mainly with respect to the identified phases and percolation / gelation. The main nonlinear material response characteristics primarily of focus are those that do not obey theoretical scaling predictions in the MAOS region. For $I_{3/1}$, this includes non-quadratic scaling with the strain amplitude, $I_{3/1} \propto \gamma_0^n, n \neq 2$, γ_0 dependence in the form of multiple scaling regions ($n = f(\gamma)$) and ω-dependence in nonlinear scaling ($n = f(\omega)$), all collectively dubbed

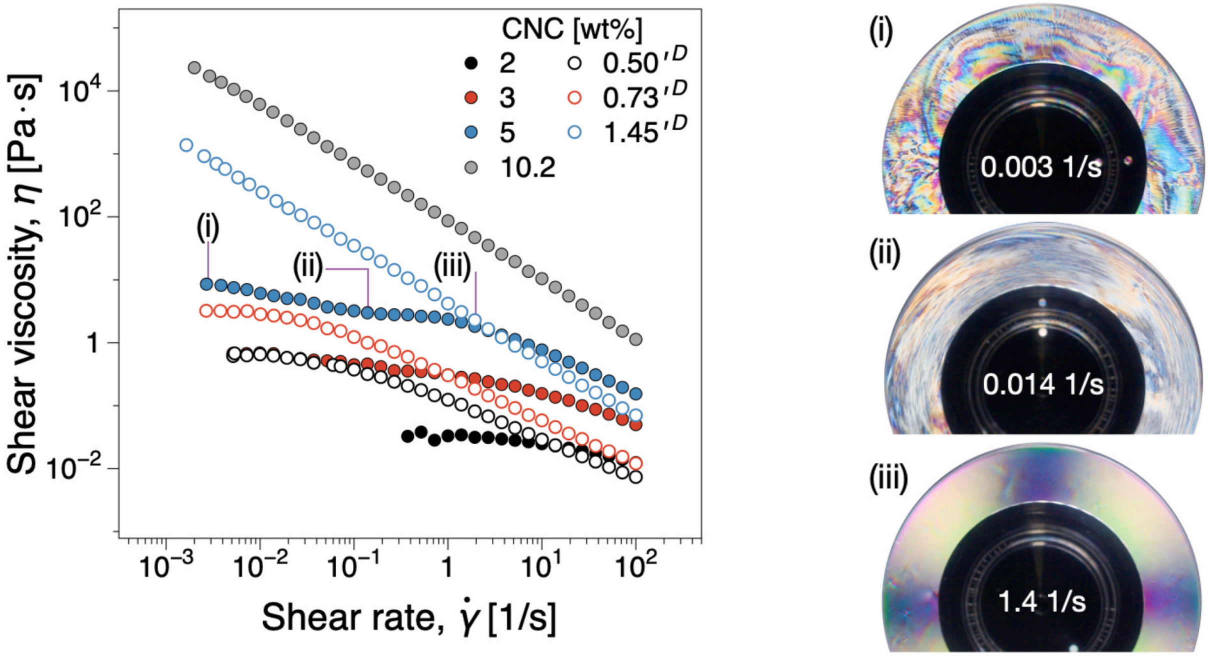

(a) (b)

Fig. 4. (a) Viscosity as function of shear rate for all investigated CNC suspensions, (b) still frames at selected shear rates for 5 wt%.

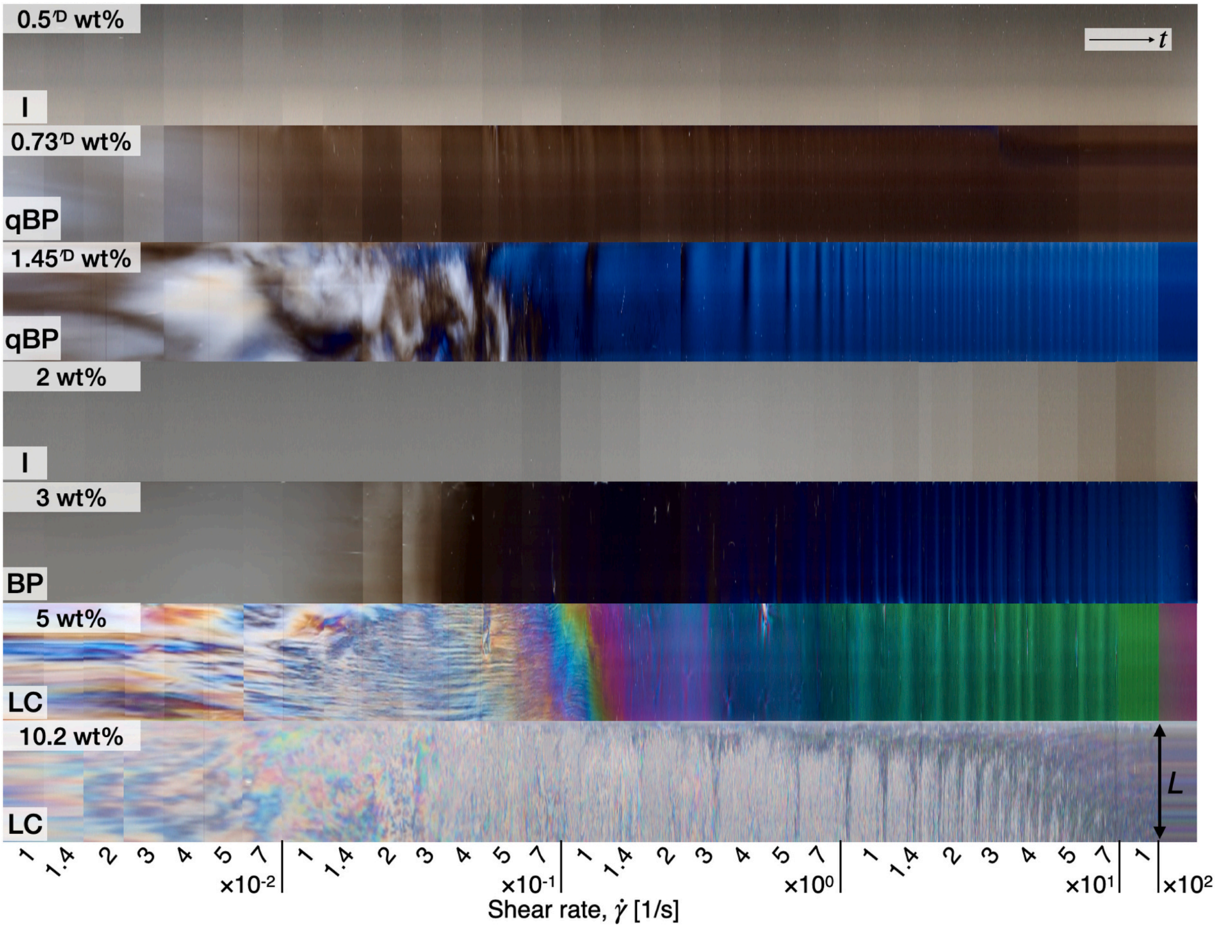

Fig. 5. Space-time optical visualization from the steady shear tests for all investigated CNC concentrations showing the birefringence patterns.

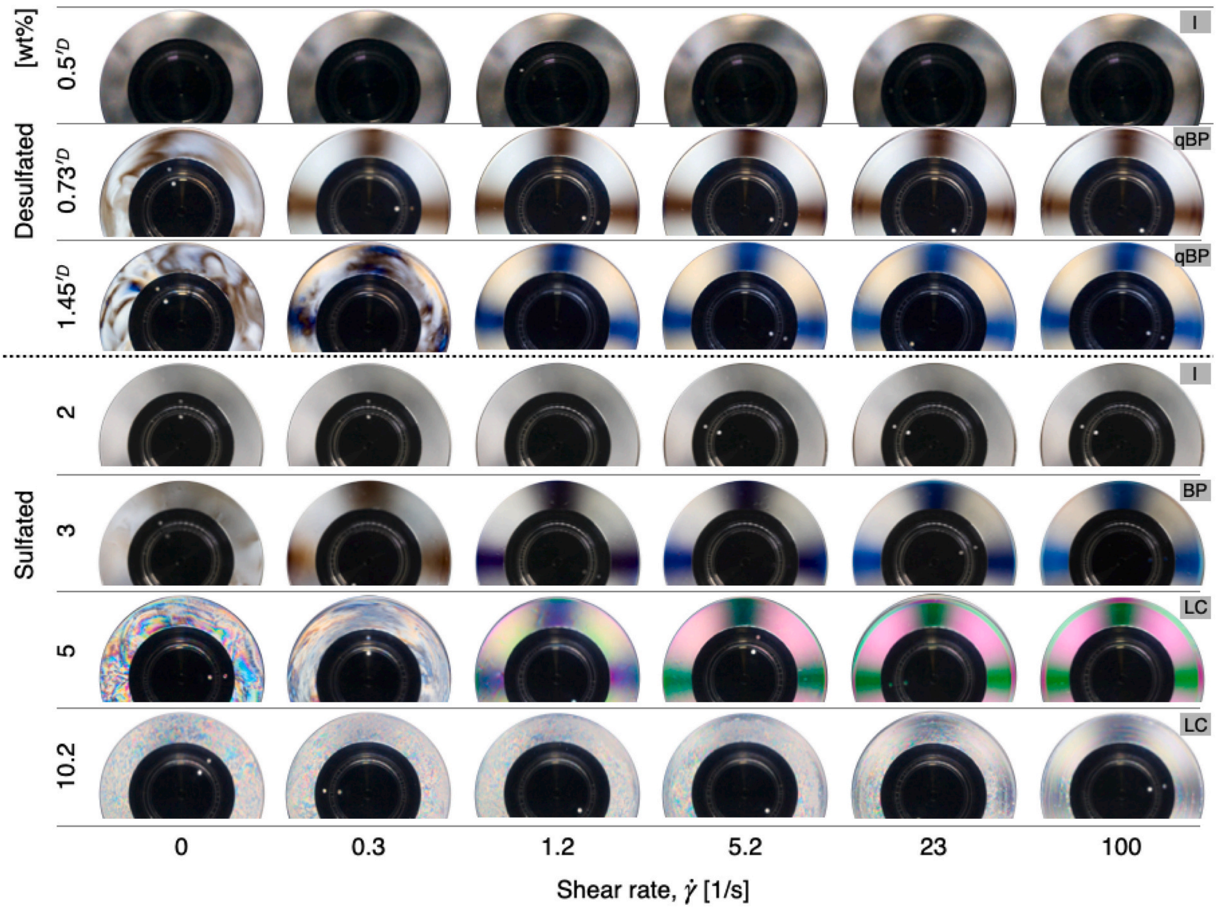

Fig. 6. Still frames showing the birefringence patterns at selected shear rates from the steady shear measurements in Fig. 4.

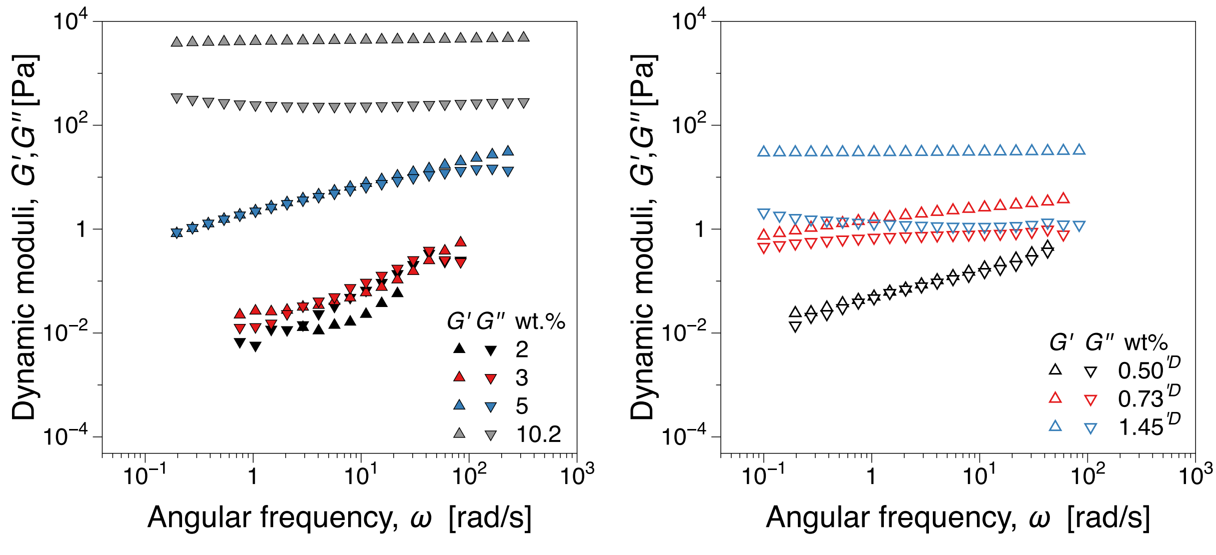

(a) (b)

Fig. 7. Dynamic moduli, G', G'' from linear viscoelastic frequency sweep measurements for (a) sulfated and (b) desulfated CNC suspensions.

nonlinear "oddities" (Kádár, Gaska, & Gkourmpis, 2020).

The nonlinear material response as expressed by the third relative higher harmonic, $I_{3/1}$ from the FT analysis of dynamic strain sweep measurements is presented in Fig. 8. The region at a very low strain amplitudes, identifiable as semitransparent data points in the figure, corresponds to instrumentation noise in the SAOS region. The 2 wt% sulfated suspension, Fig. 8(a), exhibited a single MAOS quadratic scaling region as predicted theoretically, i.e. $I_{3/1} \propto \gamma_0^n$, $n = 2$, or asymptotically tending thereto (Lim et al., 2013). This is expected for an isotropic CNC suspension below the gel point and in good agreement with similar

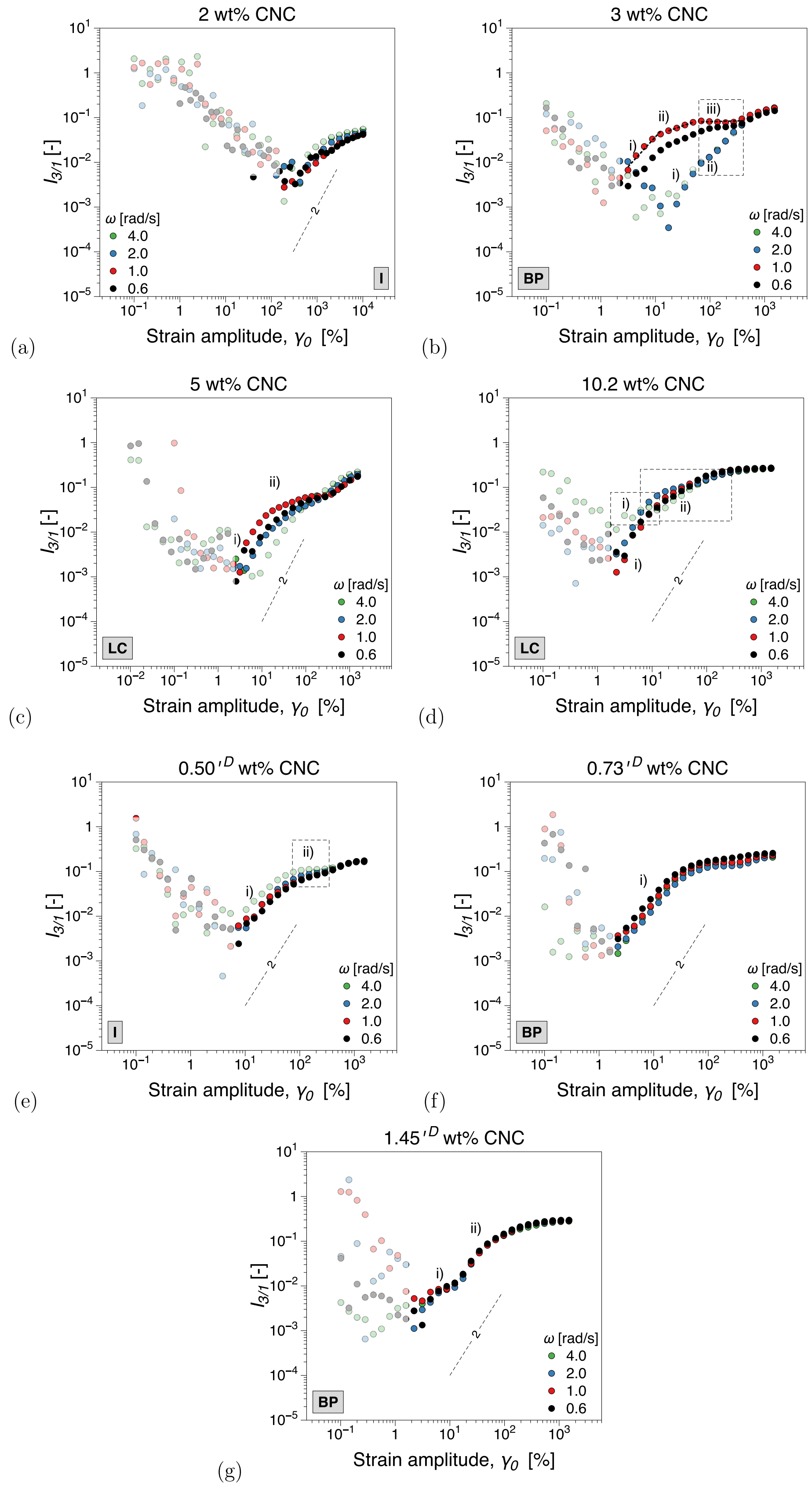

Fig. 8. Third relative higher harmonic, $I_{3/1}$, from dynamic strain sweeps for $\omega = 0.6,1,2,4$ rad/s: (a) 2 wt%, (b) 3 wt%, (c) 5 wt%, (d) 10.2 wt% CNC, (e) 0.5$'^{D}$ wt%, (f) 0.73$'^{D}$ wt%, (g) 1.45$'^{D}$ wt%.

findings in other CNC aqueous suspensions in general (Wojno et al., 2022). The apparent variation in $I_{3/1}$ magnitude with ω can be most likely attributed to low measurement torques (Wojno et al., 2022). The biphasic 3 wt% sulfated suspension, Fig. 8(b), is approaching the gel point, according to the strain sweep and frequency sweep data in Figs. SI6, 7, and Fig.7(a), and this was reflected in the nonlinear material response exhibiting ω-dependence and multiple scaling regions. Namely, for ω= 0.6 and 1 rad/s (i) $n \approx 1.33$ for $\gamma_0 \in [3, 15]$ %, (ii) $n \approx 0.42$ for $\gamma_0 \in [15, 50]$ %, (iii) $n \approx 0.03$ for $\gamma_0 \in [60{,}500]$ %. In contrast, with increasing ω, see ω= 2, 4 rad/s, (i)) $n \approx 1.47$ for $\gamma_0 \in [10, 50]$ %, (ii) $n \approx 1.14$ for $\gamma_0 \in [55{,}400]$ %. The significant variation in nonlinear scaling and magnitude of the nonlinearities together with the fact that with increasing ω the scaling becomes closer to a quadratic behavior suggests the presence of a weakly percolated and therefore fragile network disrupted by increasing ω, as observed by Wojno et al. (2022) and Kádár, Gaska, and Gkourmpis (2020). Further increasing the concentration, the liquid crystalline 5 wt%, exhibited a similar scaling behavior, however with lower ω-dependence compared to 3 wt%. Two scaling regions could be inferred for this concentration: (i) $n \approx 2$ for $\gamma_0 \in [3, 15]$ %, (ii) $n \approx 0.3$ for $\gamma_0 \in [20{,}350]$ %. As confirmed by the frequency sweep measurements, Fig. 7(a), the sample is at the rheological gel point and therefore the CNC network formed is stronger due to sufficiently high connection points between nanoparticles /mesophase such that it cannot be easily disrupted. The liquid crystalline 10.2 wt% CNC suspension exhibited the least ω-dependence, confirming the existence of a resilient gelled internal network. However, two scaling regions can be distinguished, suggesting still non-trivial nanoparticle/mesophase dynamics: (a) for ω=0.6, 1, 2 (i) $n \approx 1.94$ for $\gamma_0 \in [3, 15]$ %, (ii) $n \approx 0.64$ for $\gamma_0 \in [15{,}100]$ % and (b) for $\omega = 4$ rad/s (i) $n \approx 0.32$ for $\gamma_0 \in [3, 15]$ %, (ii) $n \approx 0.82$ for $\gamma_0 \in [13{,}100]$ %.

In contrast, the desulfated isotropic $0.5^{'D}$ showed two distinct MAOS scaling regions, for each ω. The scaling indices, see the labels in Fig. 8(e), were: i) $n \approx 1.4$ for $\gamma_0 \in [8, 60]$ % and ii) $n \approx 0.2$ for $\gamma_0 \in [80{,}200]$ %. Importantly, while the scaling behavior is similar to the sulfated isotropic 2 wt% (both are isotropic) the influence of ω is significantly reduced for the desulfated isotropic CNC suspension. This is expected considering that $0.5^{'D}$ wt% is closer to the gel point compared to 2 wt%. In addition, the effective aspect ratio of the suspensions is higher thus favoring more contact points between network forming elements and therefore it is more comparable to the sulfated 3 wt%. It can be then inferred that the isotropic desulfated $0.5^{'D}$ wt% presents a more resilient CNC network to flow induced disturbances compared to the sulfated 3 wt%. Interestingly, $0.73^{'D}$ wt%, concentration clearly above the gel point, Fig. SI7(b), is independent on applied ω and has a nearly-quadratic scaling exponent, $n \approx 2$, Fig. 8(f). Previously, we had reported the absence of nonlinear 'oddities' at some concentrations above the gel point in sulfated CNC suspensions (Wojno et al., 2022). Since in our previous study a broader range of concentrations was investigated, it was apparent that such cases are transitions between scaling exponents, i.e. compare 3–5 wt% in Wojno et al. (2022). Similarly, for the desulfated $0.73^{'D}$ wt% the weakly distorted nonlinear material response at the MAOS-LAOS transition could be evidence of a nonlinear transition state from $0.5^{'D}$ to higher concentrations. We note that for this assertion to be validated a more detailed concentration influence study would be required. The highest investigated desulfated concentration, $1.45^{'D}$ wt%, has two pronounced scaling regions but no ω-dependence: (i) $n \approx 0.5 - 0.8$ for $\gamma_0 \in [2, 10]$ % and (ii) $n \approx 1.35$ for $\gamma_0 \in [11, 90]$ %, Fig. 8(g). We note that region ii) appears approximately around the onset of WSO in linear viscoelastic strain sweeps, Fig. SI7(c)–(d), corresponding to microstructural 'jamming'. However, WSO appears also for $0.5^{'D}$ wt% and yet $I_{3/1}(\gamma_0)$ lacks a similar scaling region. The attractive interactions in desulfated $1.45^{'D}$ wt% promote agglomeration, aggregation or gelation. From the linear viscoelastic measurements it was shown that this concentration is a gel. Therefore boundaries between nanoparticles are stronger due to the capability of CNC to form an apparent continuous H-bonded three-dimensional network when its content is above the percolation (Favier et al., 1995; Mariano et al., 2016). The scaling behavior of 1.45^{D} wt% is similar to the sulfated 3 wt% CNC suspension based on the same source CNC, however with different preparation methodology (Wojno et al., 2022), and to a hybrid polymer nanocomposite (containing carbon black and graphite nanoplatelets) above the electrical percolation threshold outlined by Gaska and Kádár (2019). Correlations between the different systems are however not obvious at this time.

By comparing the nonlinear material response with PLI data from rheo-PLI experiments, some conjectures could be made regarding the origin of nonlinear phenomena, considering that PLI at the observation scale captures the mesophase and its orientation dynamics but cannot capture individual CNC interactions (Fazilati et al., 2021). The third relative higher harmonic compared with corresponding PLI still frames and space-time diagrams from rheo-PLI strain sweeps for $\omega = 1$ rad/s at two selected concentrations is presented in Fig. 9. No observable changes in the SAOS-MAOS transition region, where typically nonlinear 'oddities' occur in the PLI patterns or still frames, were recorded. Therefore, it can be conjectured that in this region structural rearrangements responsible for the nonlinear behavior involve interactions between individual nanoparticles, i.e. CNC-CNC. This can be in the form of interactions in the isotropic phase of a biphasic system, Fig. 9(a), or interactions at the boundaries between liquid crystalline domains for a liquid crystalline phase system, Fig. 9(b). We note that in the case of the desulfated $1.45^{'D}$ in Fig. 9 as the system is above the gel point, a break-up / re-connection of the axially aggregated CNCs could occur. The onset PLI color pattern distortions correspond mostly to the LAOS region, with particularities depending on the specific phase. For the desulfated biphasic $1.45^{'D}$ this occurred at approximately 30 %. This corresponded rather well to the loss of quadratic scaling in $I_3/1$ in scaling region ii). For the sulfated liquid crystalline 5 this corresponded to strain amplitudes above 80 %, that also corresponds to the end of scaling region ii) even in the absence of a quadratic scaling behavior. A Maltese-cross can be distinguished in the LAOS region at strain amplitudes above 100 %, where PLI color patterns change significantly.

Elastic and viscous Lissajous diagrams and description thereof can be found in the Supplementary information (Figs. SI9–10). The stress decomposition analysis, expressed by strain-stiffening (S) and shear-thickening (T) dimensionless ratios can be found in Fig. SI 11 for all concentrations. The lowest analyzed concentrations, due to their low viscosity result in scattered datapoints, a consequence of a low torques, as found in the previous data analyses presented. This effect is observed for isotropic sulfated 2 wt%, Fig. SI11(a). As in our previous study, all concentrations exhibit a nonlinear intra-cycle strain-stiffening, where $S > 0$. Additionally, the dominant nonlinear viscous behavior is intra-cycle shear-thinning, where $T < 0$. Interestingly, a local shear-thickening behavior, where $T > 0$, with increasing concentration, for both sulfated and desulfated CNC systems was observed. The local shear-thickening appears around 10^1 %, whereafter T drops, resulting in intra-cycle shear-thinning, $T < 0$. Similar to our previous study, this local thickening behavior was detected in nonlinear data before WSO and effectively marks the transition to biphasic phase in both sulfated and desulfated systems analyzed. The nonlinear feature is present throughout the biphasic and liquid crystalline phases. We note the absence of a local strain-softening ($S < 0$) behavior that in our previous work effectively marked the transition to the liquid crystalline phase (Wojno et al., 2022). Considering the sulfated systems, given that there is significant difference at microstructural level based on POM, e.g. 'coarse' vs. 'fine', the local strain-softening could be associated to agglomerate dynamics in our previous 'coarse' microstructure.

5. Summary and conclusions

The percolation, gelation and phase behavior in CNC suspensions were investigated with an emphasis on nonlinear material rheological parameters from oscillatory shear. The surface charge significantly

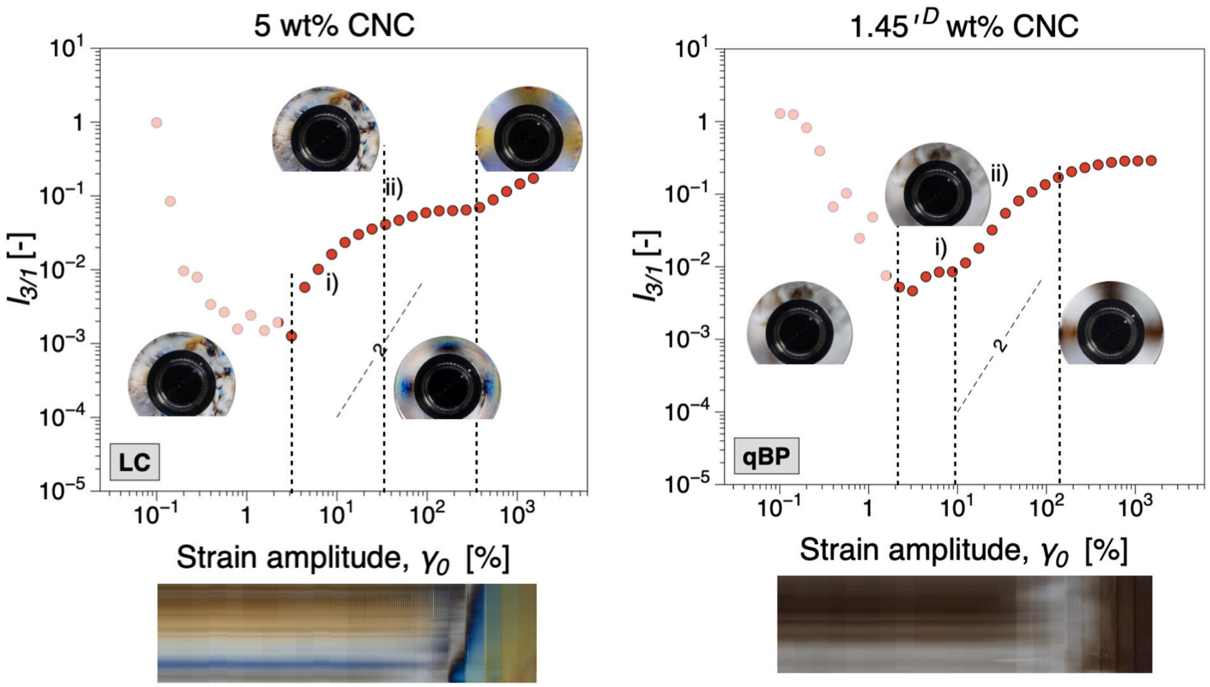

(a) (b)

Fig. 9. The third relative higher harmonic, $I_{3/1}$, from dynamic strain sweep for $\omega = 1$ rad/s compared with still frames and space-time diagrams from rheo-PLI tests for: (a) 5wt%, (b) $1.45^{\prime D}$ wt%. The vertical lines indicate the strain amplitudes the still frames correspond to.

affects the interactions between CNCs, creating the conditions to examine the significance of nonlinear material parameters. Acid desulfation decreases the surfaces charge density, which leads to an increase in attractive forces between CNCs. Consequently, sulfated and desulfated CNC systems differ in apparent nanoparticle aspect ratio, with almost three times higher effective aspect ratio for the desulfated samples. This impacts both gel formation as well as the phase behavior. A summary of the main rheological findings is presented in Fig. 10. The CNC assembly phases, isotropic (I), biphasic (BP) and liquid crystalline (LC) - were identified mainly based on POM analysis in the context of the full spectrum of characterization performed. For desulfated CNC suspensions, the isotropic phase was followed by a quasi-biphasic (qBP) state, with the latter showing BP-like behavior but not phase-separable through sedimentation tests. Thus, the gel point, ϕ_g, of sulfated CNC suspensions was identified at the transition on LC, $\phi_g = \phi_2$. In contrast, for desulfated ϕ_g could be identified at the transition to qBP, $\phi_g = \phi_1$. In both cases, the results show that the third relative higher harmonic, $I_{3/1}$, shows an anomalous behavior and the shear thickening parameter, T, shows local shear thickening behavior for $\phi < \phi_g$. While $I_{3/1} \propto \gamma^n$, $n = f(\omega, \gamma_0)$, T showed evidence of a weak strain overshoot in T in the form of a local shear thickening region, $T > 0$, before transitioning to $T < 0$. We interpret this behavior as evidence that nonlinear material parameters sensitive to the formation of a weakly percolated network in the suspensions rather, in agreement with previous findings in nanocomposite systems (Kádár, Gaska, & Gkourmpis, 2020). We therefore take this anomalous nonlinear behavior as a percolation threshold evidencing a weakly percolated network, ϕ_c, confirming the first part of our hypothesis, (i). By comparing the sulfated and desulfated samples we have effectively decoupled ϕ_c from ϕ_1. Consequently, the onset of nonlinear 'oddities' may be indicative of phase transitions, as defined in static conditions, to the extent as those are approximately equal to the critical phase transitions concentrations. Interestingly, the scaling exponent of $I_{3/1}$ remains $n = f(\omega, \gamma_0)$ even when a gel point can be detected in linear viscoelastic frequency sweep measurements. We attribute this discrepancy to the nonlinear conditions probing the structure that could be disruptive to the miscrostructure. Interestingly, above ϕ_g a quadratic scaling in $I_{3/1}$ was found, $n = 2$, for desulfated CNC samples, while for sulfated CNC the trend up to the highest concentration would suggest a gradual transition to the same behavior. A quadratic scaling as a gradual transition between two forms of nonlinear 'oddities' was observed above ϕ_g in our previous work (Wojno et al., 2022). Above this critical point, nonlinear material parameters show other features that point to distinct dynamics in the microstructure, that have yet to be explained. However, by comparing the nonlinear data with the PLI data, it would appear that nonlinear behavior for most of the MAOS region corresponds to structural contributions below the meso-scale observations possible through the PLI setup. Towards the LAOS transition, mesophase structural dynamics appear to play an increasingly significant role, while the LAOS region is dominated by uniformly oriented microstructure, as evidenced by the Maltese-cross pattern. Another possible conjecture is that nonlinear oscillatory flow conditions may disrupt the LC phase through intense LC-LC domain interactions so that in dynamic conditions they effectively become BP. In our previous work (Wojno et al., 2022), LC suspensions were marked by the onset of a local strain softening behavior, $S < 0$, before a transition to strain hardening behavior $S > 0$. In our present work we observed the same however, for concentrations above the BP-LC transition, $\phi > \phi_1$, Fig. 10. This could be due to the 'coarse' microstructure, i.e. dominated by larger agglomerates in POM, in our previous work compared to the 'fine' microstructure, i.e. smaller LC domains, in the current work, in that a 'fine' microstructure may be easier to disrupt microstructurally from LC to BP. Thus, we conjecture that the second part of our hypothesis, (ii), could be valid, however, the relationship between the microstructure, anomalous nonlinear signatures, i.e. "oddities", and phase behave needs to be further investigated.

CRediT authorship contribution statement

Conceptualization
RK, TA, SW
Ideas

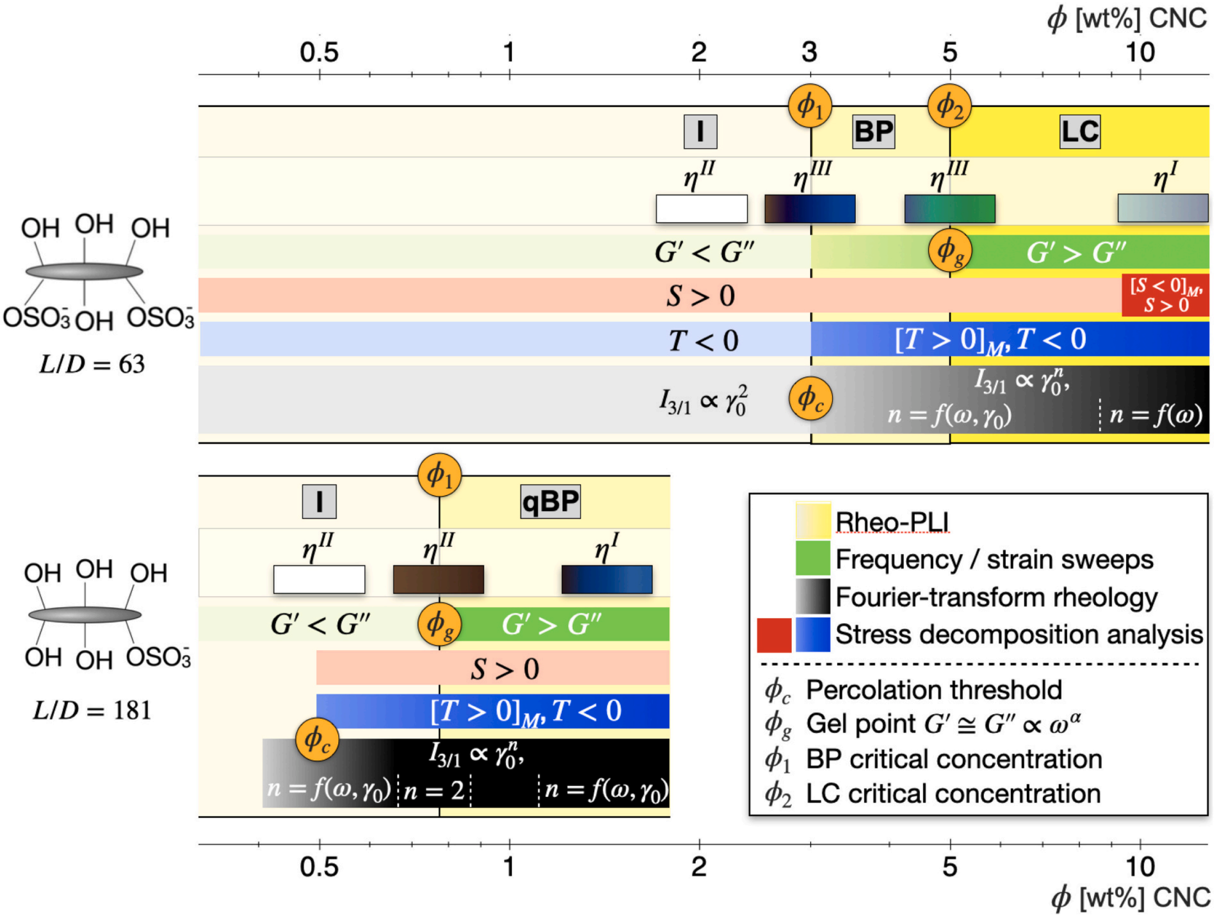

Fig. 10. Overview of rheological parameters in relation to critical concentrations. The color sequences depicted at rheo-PLI correspond to the coloring of the Maltese-cross pattern with increasing shear rate. Viscosity functions notations: η^{I} - single shear thinning region, η^{II} - zero-shear viscosity followed by a shear thinning region, and η^{III} - so-called three-region viscosity function. Subscript M indicates that the nonlinear behavior is characteristic of the MAOS region.

RK, TA
Methodology
SW, TA, RK, MAS
Investigation Conducting a research and investigation process, specifically performing the experiments, or data/evidence collection
SW, AhA, AA
Writing - Original Draft
SW, RK, AhA
Writing - Review & Editing
RK, TA, MS
Visualization
SW, RK, AhA
Supervision
RK, TA, MS
Project administration
RK
Funding acquisition
RK, TA, MS

Declaration of competing interest

The authors declare that they have no known competing financial interests or personal relationships that could have appeared to influence the work reported in this paper.

Data availability

Data will be made available on request.

Acknowledgement

SW and RK are grateful for the financial support of the Wallenberg Wood Science Centre (WWSC) and of the Chalmers Area of Advance Materials Science. The Chair of Sustainable Packaging within the Institute of Materials at EPFL, co-funded by BASF, Logitech, Nestlé and SIG, is acknowledged by TA. A.Ah, A.A. and M.S. are grateful for the financial support from KP Nanocellulose platform at RISE AB.

Appendix A. Supplementary data

Supplementary data to this article can be found online at https://doi.org/10.1016/j.carbpol.2023.120622.

References

Abbasi Moud, A., Kamkar, M., Sanati-Nezhad, A., Hejazi, S. H., & Sundararaj, U. (2020). Nonlinear viscoelastic characterization of charged cellulose nanocrystal network structure in the presence of salt in aqueous media. *Cellulose, 27*, 5729–5743.

Abitbol, T., Kam, D., Levi-Kalisman, Y., Gray, D. G., & Shoseyov, O. (2018). Surface charge influence on the phase separation and viscosity of cellulose nanocrystals. *Langmuir, 34*, 3925–3933.

Abitbol, T., Palermo, A., Moran-Mirabal, J. M., & Cranston, E. D. (2013). Fluorescent labeling and characterization of cellulose nanocrystals with varying charge contents. *Biomacromolecules, 14*, 3278–3284.

Ao, G., Davis, V. A., Kitchens, C. L., & Ureña-Benavides, E. E. (2011). Rheology and phase behavior of lyotropic cellulose nanocrystal suspensions. *Macromolecules, 44*, 8990–8998.

Araki, J. (2013). Electrostatic or steric? – preparations and characterizations of well-dispersed systems containing rod-like nanowhiskers of crystalline polysaccharides. *Soft Matter, 9*, 4125–4141.

Araki, J., Wada, M., Kuga, S., & Okano, T. (1998). Flow properties of microcrystalline cellulose suspension prepared by acid treatment of native cellulose. *Colloids and Surfaces A: Physicochemical and Engineering Aspects, 142*, 75–82.

Araki, J., Wada, M., Kuga, S., & Okano, T. (1999). Influence of surface charge on viscosity behavior of cellulose microcrystal suspension. *Journal of Wood Science, 45*, 258–261.

Araki, J., Wada, M., Kuga, S., & Okano, T. (2000). Birefringent glassy phase of a cellulose microcrystal suspension. *Langmuir, 16*, 2413–2415.

Bercea, M., & Navard, P. (2000). Shear dynamics of aqueous suspensions of cellulose whiskers. *Macromolecules, 33*, 6011–6016.

Bhattacharjee, S. (2016). DLS and zeta potential –What they are and what they are not? *Journal of Controlled Release, 235*, 337–351.

Buining, P. A., Philipse, A. P., & Lekkerkerker, H. N. W. (1994). Phase behavior of aqueous dispersions of colloidal boehmite rods. *Langmuir, 10*, 2106–2114.

Carlos, G. L., & Walter, R. (2021). Oscillatory rheology of carboxymethyl cellulose gels: Influence of concentration and pH. *Carbohydrate Polymers, 267*, 118117.

Dong, X. M., Kimura, T., Revol, J.-F., & Gray, D. G. (1996). Effects of ionic strength on the Isotropicâ˘Chiral nematic phase transition of suspensions of cellulose crystallites. *Langmuir, 12*, 2076–2082.

Dong, X. M., Revol, J.-F., & Gray, D. G. (1998). Effect of microcrystallite preparation conditions on the formation of colloid crystals of cellulose. *Cellulose, 5*, 19–32.

Dufresne, A. (2017). *Nanocellulose: From nature to high performance tailored materials*. Walter de Gruyter GmbH.

Favier, V., Canova, G., Cavaillé, J.-Y., Chanzy, H., Dufresne, A., & Gauthier, C. (1995). Nanocomposite materials from latex and cellulose whiskers. *Polymers for Advanced Technologies, 5*, 351–355.

Fazilati, M., Ingelsten, S., Wojno, S., Nypelö, T., & Kádár, R. (2021). Thixotropy of cellulose nanocrystal suspensions. *Journal of Rheology, 65*.

Gabriel, J.-C. P., Sanchez, C., & Davidson, P. (1996). Observation of nematic liquid-crystal textures in aqueous gels of smectite clays. *The Journal of Physical Chemistry, 100*, 11139–11143.

Gaska, K., & Kádár, R. (2019). Evidence of percolated network at the linear -nonlinear transition in oscillatory shear. *AIP Conference Proceedings, 2107*, Article 050003.

Habibi, Y., Lucia, L. A., & Rojas, O. J. (2010). Cellulose nanocrystals: Chemistry, self-assembly, and applications. *Chemical Reviews, 110*, 3479–3500.

Hausmann, M. K., Rühs, P. A., Siqueira, G., Läuger, J., Libanori, R., Zimmermann, T., & Studart, A. R. (2018). Dynamics of cellulose nanocrystal alignment during 3D printing. *ACS Nano, 12*, 6926–6937.

Haywood, A. D., Weigandt, K. M., Saha, P., Noor, M., Green, M. J., & Davis, V. A. (2017). New insights into the flow and microstructural relaxation behavior of biphasic cellulose nanocrystal dispersions from RheoSANS. *Soft Matter, 13*, 8451–8462.

Hyun, K., & Kim, W. (2011). A new non-linear parameter Q from FT-rheology under nonlinear dynamic oscillatory shear for polymer melts system. *Korea-Australia Rheology Journal, 23*, 227–235.

Hyun, K., Wilhelm, M., Klein, C. O., Cho, K. S., Nam, J. G., Ahn, K. H., Lee, S. J., Ewoldt, R. H., & McKinley, G. H. (2011). A review of nonlinear oscillatory shear tests: Analysis and application of large amplitude oscillatory shear (LAOS). *Progress in Polymer Science, 36*, 1697–1753.

Jiang, F., Esker, A. R., & Roman, M. (2010). Acid-catalyzed and solvolytic desulfation of H2SO4-hydrolyzed cellulose nanocrystals. *Langmuir, 26*, 17919–17925.

Kádár, R., Fazilati, M., & Nypelö, T. (2020). Unexpected microphase transitions in flow towards nematic order of cellulose nanocrystals. *Cellulose, 27*, 2003–2014.

Kádár, R., Gaska, K., & Gkourmpis, T. (2020). Nonlinear, "oddities" at the percolation of 3D hierarchical graphene polymer nanocomposites. *Rheologica Acta, 59*, 333–347.

Kádár, R., Spirk, S., & Nypelö, T. (2021). Cellulose nanocrystal liquid crystal phases: Progress and challenges in characterization using rheology coupled to optics, scattering, and spectroscopy. *ACS Nano, 15*, 7931–7945.

Kaushik, M., Chen, W. C., van de Ven, T. G. M., & Moores, A. (2014). An improved methodology for imaging cellulose nanocrystals by transmission electron microscopy. *Nordic Pulp & Paper Research Journal, 29*, 77–84.

Lim, H. T., Ahn, K. H., Hong, J. S., & Hyun, K. (2013). Nonlinear viscoelasticity of polymer nanocomposites under large amplitude oscillatory shear flow. *Journal of Rheology, 57*, 767–789.

Mariano, M., Chirat, C., El Kissi, N., & Dufresne, A. (2016). Impact of cellulose nanocrystal aspect ratio on crystallization and reinforcement of poly (butylene adipate-co-terephthalate). *Journal of Polymer Science Part B: Polymer Physics, 54*, 2284–2297.

Moud, A. A., Kamkar, M., Sanati-Nezhad, A., Hejazi, S. H., & Sundararaj, U. (2021). Viscoelastic properties of poly (vinyl alcohol) hydrogels with cellulose nanocrystals fabricated through sodium chloride addition: Rheological evidence of double network formation. *Colloids and Surfaces A: Physicochemical and Engineering Aspects, 609*, Article 125577.

Onogi, S., & Asada, T. (1980). Chapter rheology and rheo-optics of polymer liquid crystals. In *Rheology: Volume 1: Principles*. US: Springer.

Orts, W. J., Godbout, L., Marchessault, R. H., & Revol, J. F. (1998). Enhanced ordering of liquid crystalline suspensions of cellulose microfibrils: A small angle neutron scattering study. *Macromolecules, 31*, 5117–5725.

Parker, R. M., Guidetti, G., Williams, C. A., Zhao, T., Narkevicius, A., Vignolini, S., & Frka-Petesic, B. (2018). The self-assembly of cellulose nanocrystals: Hierarchical design of visual appearance. *Advanced Materials, 30*, 1704477.

Qi, W., Xu, H.-N., & Zhang, L. (2005). The aggregation behavior of cellulose micro/nanoparticles in aqueous media. *RSC Advances, 15*, 8770–8777.

Reid, M. S., Villalobos, M., & Cranston, E. D. (2017). Benchmarking cellulose nanocrystals: From the laboratory to industrial production. *Langmuir, 33*, 1583–1598.

Shafeiei-Sabet, S., Hamad, W. Y., & Hatzikiriakos, S. G. (2013). Influence of degree of sulfation on the rheology of cellulose nanocrystal suspensions. *Rheologica Acta, 52*, 741–751.

Shafiei-Sabet, S., Hamad, W. Y., & Hatzikiriakos, S. G. (2012). Rheology of nanocrystalline cellulose aqueous suspensions. *Langmuir, 28*, 17124–17133.

Shafiei-Sabet, S., Hamad, W. Y., & Hatzikiriakos, S. G. (2014). Ionic strength effects on the microstructure and shear rheology of cellulose nanocrystal suspensions. *Cellulose, 21*, 3347–3359.

Song, H. Y., Park, S. Y., Kim, S., Youn, H. J., & Hyun, K. (2022). Linear and nonlinear oscillatory rheology of chemically pretreated and non-pretreated cellulose nanofiber suspensions. *Carbohydrate Polymers, 275*, Article 118765.

Völker-Pop, L. (2014). Optical methods in rheology: Polarized light imaging. *Chemicke Listy, 108*, 697–724.

Winter, H. H., & Chambon, F. (1986). Analysis of linear viscoelasticity of a crosslinking polymer at the gel point. *Langmuir, 30*, 367–382.

Wojno, S., Westman, G., & Kádár, R. (2019). Gel point in CNC dispersion from FT rheology. In *, 27. Conference: Annual transactions of the Nordic Rheology Society* (pp. 179–184).

Wychowaniec, J., Iliut, M., Borek, B., Muryn, C., Mykhaylyk, O. O., Edmondson, S., & Vijayaraghavan, A. (2021). Elastic flow instabilities and macroscopic textures in graphene oxide lyotropic liquid crystals. *npj 2D Materials and Applications, 5*, 545–570.

Xu, Y., Atrens, A., & Stokes, J. R. (2020). A review of nanocrystalline cellulose suspensions: Rheology, liquid crystal ordering and colloidal phase behaviour. *Advances in Colloid and Interface Science, 275*, Article 102076.

Xu, Y., Atrens, A. D., & Stokes, J. R. (2017). Rheology and microstructure of aqueous suspensions of nanocrystalline cellulose rods. *Journal of Colloid and Interface Science, 496*, 130–140.

Xu, Y., Atrens, A. D., & Stokes, J. R. (2018). "Liquid, gel and soft glass" phase transitions and rheology of nanocrystalline cellulose suspensions as a function of concentration and salinity. *Soft Matter, 14*, 1953–1963.

Wojno, S., Fazilati, M., Nypelö, T., Westman, G., & Kádár, R. (2022). Phase transitions of cellulose nanocrystal suspensions from nonlinear oscillatory shear. *Cellulose, 29*, 3655–3673.